

pubs.acs.org/JCTC Article

Attosecond Monitoring of Nonadiabatic Molecular Dynamics by Transient X-ray Transmission Spectroscopy

Stefano M. Cavaletto,*,¶ Yeonsig Nam,*,¶ Jérémy R. Rouxel, Daniel Keefer, Haiwang Yong, and Shaul Mukamel*



Cite This: J. Chem. Theory Comput. 2023, 19, 2327-2339



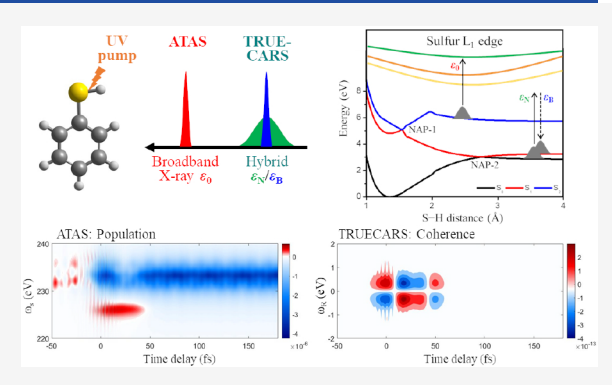
ACCESS I

III Metrics & More

Article Recommendations

s Supporting Information

ABSTRACT: Tracing the evolution of molecular coherences can provide a direct, unambiguous probe of nonadiabatic molecular processes, such as the passage through conical intersections of electronic states. Two techniques, attosecond transient absorption spectroscopy (ATAS) and Transient Redistribution of Ultrafast Electronic Coherences in Attosecond Raman Signals (TRUECARS), have been used or proposed for monitoring nonadiabatic molecular dynamics. Both techniques employ the transmission of a weak attosecond extremeultraviolet or X-ray probe to interrogate the molecule at controllable time delays with respect to an optical pump, thereby extracting dynamical information from transient spectral features. The connection between these techniques has not been firmly established yet. In this theoretical study, we provide a unified description of both transient transmission



techniques, establishing their relationship as limits of the same pump—probe spectroscopy technique for different pulse parameter regimes. We demonstrate this by quantum dynamical simulations of thiophenol photodissociation and show how complementary coherence information can be revealed by the two techniques.

1. INTRODUCTION

Nonadiabatic transitions in molecules take place when the electronic and nuclear motions become strongly coupled, leading to the breakdown of the adiabatic (Born–Oppenheimer) approximation, which allows the separate treatment of electronic and nuclear dynamics. This gives rise to finite coupling elements between energetically close electronic states, allowing for a molecular wavepacket (WP) to propagate from one state into another. The abundance, efficiency, and accessibility of such regions, often taking the shape of conical intersections (CIs) or avoided crossings (ACs), are crucially important for determining the rates and outcomes of a large class of photoinduced molecular processes. However, despite their prominent role in photochemistry and photophysics, identifying direct experimental signatures of these nonadiabatic passages (NAPs) has been very challenging. 3,4

The advent of attosecond extreme-ultraviolet (XUV) and soft- to hard-X-ray pulses from high-order harmonic generation^{5,6} and free-electron lasers^{7–9} is enabling a new arsenal of time-resolved spectroscopy techniques, which include time-resolved X-ray absorption, diffraction, and photoelectron spectroscopy. Thanks to their short duration, broad bandwidth, and high frequency, attosecond X-ray pulses are ideal for monitoring and imaging ultrafast electronic and nuclear dynamics in molecules.

Pump—probe absorption and emission techniques have been intensely investigated in theory and experimental studies of nonadiabatic dynamics in molecules. 10–13 Two time-resolved X-ray techniques have received particular attention for monitoring nonadiabatic transitions at CIs and ACs: atto-second transient absorption spectroscopy (ATAS) 14–16 and the Transient Redistribution of Ultrafast Electronic Coherences in Attosecond Raman Signals (TRUECARS). 17–19 Both employ the same pump—probe setup, where an ultraviolet/visible (UV/vis) pump pulse launches some ultrafast dynamics, and a subsequent XUV or X-ray probe pulse monitors them via transient changes in its transmission spectrum at controllable time delays.

In ATAS, ^{14–16} the probe XUV pulse is resonant with specific high-energy transitions in the material, due to, e.g., inner-core excitations. This results in the absorption of a photon and in the appearance of absorption lines in the spectrum of the transmitted probe, centered around resonant transition energies. Transient changes in the absorption profile with the

Received: January 13, 2023 Published: April 4, 2023





pump-probe delay encode the system's dynamics. The technique has been successfully applied to study the ultrafast dynamics of atoms, ^{20–24} molecules, ^{25–34} and solids. ^{35–39} It has also been implemented to monitor nonadiabatic dynamics at CIs. 27-31,33,34 In these works, the NAP was inferred from the transient appearance of new absorption lines or from the splitting of existing ones. These spectral features are determined by the evolution of state populations, i.e., the probabilities with which different electronic states are occupied. These populations are not a direct indicator of nonadiabatic dynamics, as state population will always be present, independent of the occurrence or absence of NAPs. Coherence dynamics can be additionally encoded in the ATAS signal via modulations in the absorption amplitudes, 16 but coherence contributions are typically weaker than, and are thus hidden beneath, contributions from state populations, especially at the NAP. Unambiguously ascribing a given ATAS spectral feature to a NAP thus requires a detailed analysis.

TRUECARS has been proposed as an alternative technique for detecting NAPs. 17-19 Here, an off-resonant probe pulse monitors the excited-state dynamics by inducing an instantaneous stimulated Raman process between two electronic states. In the absence of a resonant high-energy excited state, real photons are not absorbed, but rather gain and loss are redistributed in different spectral regions of the transmitted probe pulse. The TRUECARS signal requires the vibronic states to be in a coherent superposition. When a NAP takes place and a coherence is generated between the states involved in the nonadiabatic transition, an unambiguous signature of the NAP appears in this signal.

In spite of the identical transmission measurement setup employed in both techniques, and despite numerous experimental and theoretical studies, the relationship between ATAS and TRUECARS has thus far not been fully established. The (apparently) distinct mechanisms involved in the two techniques—absorption for ATAS, and Stokes and anti-Stokes Raman excitations for TRUECARS—have contributed to this ambiguity. Here, we derive general expressions for the transient transmission spectroscopy (TTS) signal of a weak probe, and show that ATAS and TRUECARS are special cases of the same technique, for a resonant or an off-resonant probe, respectively. By unveiling the relationship between the two techniques, our unified description should greatly benefit the deciphering of the crucial role of NAPs in photochemistry from complementary angles of the same transient transmission setup. We exemplify this for the photodissociation dynamics of thiophenol molecules involving two electronic state crossings, with simulations showing the complementary dynamical information on state populations and coherences accessed by the two techniques. Understanding the precise connection between ATAS and TRUECARS should help developments in their experimental implementation and interpretation. Our approach can be extended to other time-resolved spectroscopies, and can thus stimulate the development of novel TTS techniques with near-resonant probe pulses.

2. THE TRANSIENT TRANSMISSION SIGNAL

Expressions for the ATAS⁴⁰ and TRUECARS¹⁷ signals have been previously presented separately, without highlighting the connection between the two techniques, but rather stressing the distinct absorption and Raman-excitation processes involved in ATAS and TRUECARS, respectively. In this

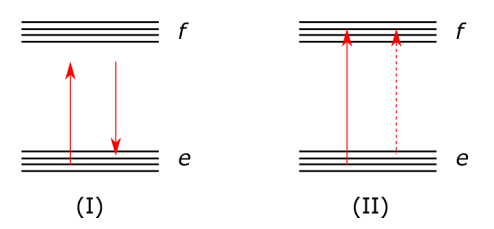


Figure 1. Electronic states involved in the X-ray TTS signal. The index e runs over the electronic ground g and valence-excited v states, while f runs over the core-excited states in the molecule. The action of the probe pulse can be visualized in two equivalent ways, i.e., (I) as a Raman process (one upward and one downward arrow) between two e states, either off- or on-resonance to the core states f, or (II) as an absorption process (two upward arrows) from e into f, with continuous lines indicating ket excitation and dashed lines bra excitation. (I) and (II) are two equivalent ways to interpret the same physical process, compare also Figures 2(I) and 2(II).

section, we derive expressions for the most general TTS signal. This allows us to show that the signal can be interpreted *both* as an absorption or a Raman process, providing a unifying picture for the two techniques.

2.1. Definition of the TTS Signal. The TTS setup involves a weak probe pulse with a variable arrival time T, used to monitor the nonstationary state of a molecular WP undergoing a NAP. A UV/vis pump pulse populates some electronic valence states in the molecule, whose subsequent state is described by the molecule's density matrix $\hat{\rho}^{\rm M}(t) = |\Psi(t)\rangle\langle\Psi(t)|$. In the following derivation, we do not include the pump explicitly, and only focus on the action of the X-ray probe. We expand $|\Psi(t)\rangle = \sum_{e} c_e(t) |\chi_e(t)\rangle |\phi_e\rangle$ in the adiabatic electronic-state basis $\{|\phi_e\rangle\}$. Here, $|\chi_e(t)\rangle$ is the timedependent normalized nuclear WP on the eth valence-state potential-energy surface (PES) and $c_e(t)$ is its amplitude, $\sum_{e} |c_{e}(t)|^{2} = 1$. The electronic states involved in the TTS signal are shown in Figure 1, with the index e running over the electronic ground g and valence-excited ν states, and f running over the core-excited molecular states.

The frequency- and time-resolved TTS signal is obtained by measuring the variation in the absorption spectrum of the X-ray probe pulse as a function of its arrival time T. At every T, the signal is defined as the change in the frequency-dispersed transmitted probe pulse, i.e., the time-integrated rate of change of the number of photons at the probe signal frequency ω_{sp}

$$S(\omega_{\rm s}) = \int {\rm d}t \left\langle \frac{{\rm d}\hat{N}(\omega_{\rm s})}{{\rm d}t} \right\rangle \tag{1}$$

Here, $\hat{N}(\omega_{\rm s})=\hat{a}^{\dagger}(\omega_{\rm s})\hat{a}(\omega_{\rm s})$ is the number operator of a photon with the detected frequency $\omega_{\rm s}$, written in terms of the associated creation and annihilation operators, $\hat{a}^{\dagger}(\omega_{\rm s})$ and $\hat{a}(\omega_{\rm s})$, respectively. $\langle \hat{A} \rangle$ denotes the expectation value of a generic operator \hat{A} . Here and in the following, atomic units are used.

2.2. Derivation of the TTS Signal. The expressions of the TTS signal are derived by solving Heisenberg's equations of motion for the photon-number operator $\hat{N}(\omega_s)$,

$$\frac{\mathrm{d}\hat{N}(\omega_{\mathrm{s}})}{\mathrm{d}t} = \mathrm{i}[\hat{H}_{\mathrm{int}}, \, \hat{N}(\omega_{\mathrm{s}})] \tag{2}$$

with the probe-matter interaction Hamiltonian in the dipole and the rotating-wave approximation,

$$\hat{H}_{\text{int}} = -\hat{\mathbf{E}} \cdot \hat{\mathbf{V}}^{\dagger} - \hat{\mathbf{E}}^{\dagger} \cdot \hat{\mathbf{V}}$$
(3)

$$\hat{\mathbf{E}} = \hat{\mathbf{e}} \sum_{j} i \sqrt{\frac{2\pi\omega_{j}}{\Omega}} \, \hat{a}(\omega_{j}) \tag{4}$$

and $\hat{\mathbf{E}}^{\mathsf{T}}$ are the positive- and negative-frequency components of the probe electric-field operator, Ω is the quantization volume, $\hat{\mathbf{e}}$ the polarization unit vector, and the index j runs over the modes of the probe pulse. $\hat{a}(\omega_i)$, $\hat{a}^{\dagger}(\omega_i)$, and $\hat{N}(\omega_i) = \hat{a}^{\dagger}(\omega_i)\hat{a}(\omega_i)$ are the bosonic annihilation, creation, and number operators of a photon in the jth mode, with bosonic commutation relations $[\hat{a}(\omega_i), \hat{a}^{\dagger}(\omega_{i'})] = \delta_{ii'}$. In eq 3,

$$\hat{\mathbf{V}} = \sum_{ef} \hat{\mathbf{V}}_{ef} |\phi_e\rangle \langle \phi_f| \tag{5}$$

is the lowering component of the dipole-moment operator, where $\hat{\mathbf{V}}_{et}$ is a lowering operator acting on the nuclear space, with the index e running over the electronic ground g and valence-excited v states, and f running over the core-excited states in the molecule (see Figure 1). $\hat{\mathbf{V}}^{\dagger}$ and $\hat{\mathbf{V}}_{et}^{\dagger}$ are the corresponding raising operators from the ground/valence e to the core *f* states.

We exploit the commutation relations of the creation and annihilation operators, and recast Heisenberg's equation of motion as

$$\left\langle \frac{\mathrm{d}\hat{N}(\omega_{\mathrm{s}})}{\mathrm{d}t} \right\rangle = -2\mathrm{Im}\{\langle \hat{E}_{\mathrm{s}}^{\dagger}(t)\hat{\mathbf{V}}(t)\cdot\hat{\mathbf{e}}^{*}\rangle\} \tag{6}$$

where we have introduced the component of the signal electric-field operator

$$\hat{E}_{\rm s} = i\sqrt{\frac{2\pi\omega_{\rm s}}{\Omega}}\,\hat{a}(\omega_{\rm s})\tag{7}$$

The temporal dependence of eq 6 can be expressed in the interaction picture,

$$\begin{split} \langle \hat{E}_{s}^{\dagger}(t) \hat{\mathbf{V}}(t) \cdot \hat{\mathbf{e}}^{*} \rangle &= \mathrm{Tr} \{ \hat{E}_{s,\mathrm{I}}^{\dagger}(t) \hat{\mathbf{V}}_{\mathrm{I}}(t) \cdot \hat{\mathbf{e}}^{*} \hat{\mathbb{Q}}_{\mathrm{I}}(t) \} \\ &= \mathrm{Tr} \Big\{ \hat{E}_{s,\mathrm{I}}^{\dagger}(t) \hat{\mathbf{V}}_{\mathrm{I}}(t) \cdot \hat{\mathbf{e}}^{*} \mathcal{T} e^{-\mathrm{i} \int_{-\infty}^{t} \mathrm{d}t' \hat{\mathcal{H}}_{\mathrm{int,I,-}}(t')} \\ &\times \hat{\mathbb{Q}}_{\mathrm{I}}(-\infty) \Big\} \end{split}$$

$$(8)$$

where the subscript I denotes interaction-picture operators, \mathcal{T} denotes the time ordering of operators, $\hat{\varrho}_{r}(t)$ is the density matrix of the total system consisting of the molecule and the probe field, and $\hat{\mathcal{H}}_{\text{int.I.-}}$ is the Liouville superoperator described by $\hat{\mathcal{H}}_{\text{int,I}}$, $\hat{\mathcal{Q}}_{\text{I}} = [\hat{H}_{\text{int,I}}, \hat{\mathcal{Q}}_{\text{I}}]$. To first order in \hat{H}_{int} , eq 8 can be recast as

$$\langle \hat{E}_{s}^{\dagger}(t)\hat{\mathbf{V}}(t)\cdot\hat{\mathbf{e}}^{*}\rangle$$

$$= \operatorname{Tr}\left\{\hat{E}_{s,I}^{\dagger}(t)\hat{\mathbf{V}}_{I}(t)\cdot\hat{\mathbf{e}}^{*}\right\}$$

$$\times i \int_{0}^{\infty} dt_{I}\hat{E}_{I}(t-t_{I})\hat{\mathbf{V}}_{I}^{\dagger}(t-t_{I})\cdot\hat{\mathbf{e}}\hat{\mathbf{Q}}_{I}(-\infty)\right\}$$
(9)

where we have assumed a UV/vis pump pulse, so that the initial state of the molecule is given by a superposition of ground/valence-excited states and does not include the core states f. Had a resonant X-ray pump pulse been used, then stimulated emission from the core-excited state would have additionally contributed to the signal.

To derive closed-form expressions for the signal, we assume that the molecule and the field are initially in uncorrelated states, $\hat{Q}_{I}(t) = \hat{\rho}_{I}^{M}(t) \prod_{i} \hat{\rho}_{i,I}^{F}(t)$, with the *j*th-mode field's density matrix $\hat{\rho}_{i,I}^{F}(t)$. The trace in eq 9 then factorizes as the product of two traces, over the field and molecule's degrees of freedom:

$$\langle \hat{E}_{s}^{\dagger}(t)\hat{\mathbf{V}}(t)\cdot\hat{\mathbf{e}}^{*}\rangle$$

$$= \int_{0}^{\infty} dt_{1} \operatorname{Tr} \left\{ \hat{E}_{s,1}^{\dagger}(t)\hat{E}_{1}(t-t_{1}) \prod_{j} \hat{\rho}_{j,1}^{F}(-\infty) \right\}$$

$$\times i \operatorname{Tr} \{\hat{\mathbf{V}}_{I}(t)\cdot\hat{\mathbf{e}}^{*}\hat{\mathbf{V}}_{1}^{\dagger}(t-t_{1})\cdot\hat{\mathbf{e}}\hat{\rho}_{1}^{M}(-\infty) \}$$
(10)

To calculate the expectation value over the field's degrees of freedom in eq 10, we model the state of each field's mode by a coherent state $\hat{\rho}_{i,I}^{F}(t) = |\alpha_{i,I}(t)\rangle\langle\alpha_{i,I}(t)|$. Here, $|\alpha_{i}\rangle$ is defined as the eigenstate of the corresponding annihilation operator, $\hat{a}(\omega_i)|\alpha_i\rangle = \alpha_i|\alpha_i\rangle$. The expectation value of the electric-field operator $\langle \hat{E}_{I}(t) \rangle = E(t)$ thus reduces to the classical electric field E(t). Hereafter, we assume a probe pulse of the form

$$E(t) = \mathcal{E}(t - T)e^{-i\omega_0(t - T)} \tag{11}$$

with envelope $\mathcal{E}(t)$, central frequency ω_0 , and central time T. We also introduce the Fourier transform of the pulse envelope, $\tilde{\mathcal{E}}(\omega) = \int \mathrm{d}t \mathcal{E}(t) \mathrm{e}^{\mathrm{i}\omega t}$ and of the total probe field, $\tilde{E}(\omega) = \int dt E(t) e^{i\omega t} = \tilde{E}(\omega - \omega_0) e^{i\omega T}$. With these definitions, the expectation value of the signal component of the electric field $\hat{E}_{s,I}(t)$ is given by $\langle \hat{E}_{s,I}(t) \rangle = \tilde{E}(\omega_s) e^{-i\omega_s t}$.

The expectation value over the molecular degrees of freedom in eq 10 are calculated by moving from the interaction to the Schrödinger picture, and by exploiting the definition of the molecular state, $\hat{\rho}^{\rm M}(t) = |\Psi(t)\rangle\langle\Psi(t)|$. By inserting this into the definition of the signal (eq 1), we obtain the final formal expression for the frequency- and time-dependent TTS signal as

$$S(\omega_{s}, T)$$

$$= -2\operatorname{Im}\left\{\tilde{\mathcal{E}}^{*}(\omega_{s} - \omega_{0}) \int dt \int_{0}^{\infty} dt_{1}\mathcal{E}(t - t_{1} - T) \right.$$

$$\times e^{i(\omega_{s} - \omega_{0})(t - t_{1} - T)} e^{i\omega_{s}t_{1}}$$

$$\times i\langle \Psi(t)|\hat{\mathbf{V}} \cdot \hat{\mathbf{e}}^{*}\hat{G}_{0}(t, t - t_{1})\hat{\mathbf{V}}^{\dagger} \cdot \hat{\mathbf{e}}|\Psi(t - t_{1})\rangle \right\}$$

$$(12)$$

Here, $\hat{G}_0(t, t - t_1)$ is the molecule's free-evolution operator. The signal was here derived by using the dipole light-matter interaction Hamiltonian in eq 3, but alternatively, it could be more generally expressed in terms of charge- and current-density operators, as presented in Sec. S1 in the Supporting Information (SI).

2.3. Interpreting the TTS Signal as an Absorption or a Stimulated Raman Process. To express the dependence of the signal on the dynamics of the ground, valence, and core states involved in TTS, we expand the signal in eq 12 in the adiabatic basis as

$$S(\omega_{s}, T)$$

$$= -2\operatorname{Im}\left\{\tilde{\mathcal{E}}^{*}(\omega_{s} - \omega_{0}) \int dt \int_{0}^{\infty} dt_{1}\mathcal{E}(t - t_{1} - T) \right.$$

$$\times e^{i(\omega_{s} - \omega_{0})(t - t_{1} - T)} e^{i\omega_{s}t_{1}} \sum_{ee'f} c_{e'}^{*}(t) c_{e}(t - t_{1})$$

$$\times \left\langle \chi_{e'}(t) | \hat{\mathbf{V}}_{e'f} \cdot \hat{\mathbf{e}}^{*} \hat{\mathbf{G}}_{0,ff}(t, t - t_{1}) \hat{\mathbf{V}}_{fe}^{\dagger} \cdot \hat{\mathbf{e}} | \chi_{e}(t - t_{1}) \right\rangle \right\}$$

$$(13)$$

where $\hat{G}_{0,f}(t, t - t_1)$ is the nuclear-space operator representing the free evolution of the molecule after excitation to a core state f.

The expressions for the TTS signal, written in terms of the wave function in Hilbert space, can be read off the loop diagrams in Figure 2.⁴¹ Expressions for the signal using the density matrix in Liouville space, which allow for coupling to a bath and are described by ladder diagrams, are provided in Sec. S2 in the SI. The shaded regions in Figure 2 represent an arbitrary preparation of the system and the NAP, leading to a nonstationary superposition state $|\phi_e\rangle\langle\phi_e|$. The red arrows indicate the two interactions with the probe pulse involved in the signal. Figures 2(I) and 2(II) provide two equivalent ways to visualize the physical process involved in TTS. In Figure 2(I), the probe induces a Raman excitation from e to e' via a core state f. By taking the imaginary part in eq 13, the TTS signal splits into two terms,

$$\langle \chi_{e'}(t)|\hat{\mathbf{V}}_{e'f}\cdot\hat{\mathbf{e}}^*\hat{G}_{0,ff}(t, t-t_1)\hat{\mathbf{V}}_{fe}^{\dagger}\cdot\hat{\mathbf{e}}|\chi_{e}(t-t_1)\rangle$$
(14a)

$$\langle \chi_{e'}(t-t_1) | \hat{\mathbf{V}}_{e'f} \cdot \hat{\mathbf{e}}^* \hat{G}_{0,ff}(t-t_1, t) \hat{\mathbf{V}}_{fe}^{\dagger} \cdot \hat{\mathbf{e}} | \chi_e(t) \rangle$$
 (14b)

associated with the loop diagrams in Figures 2(I.a) and 2(I.b), respectively. In Figure 2(I.a), the field acts twice on the ket (left branch in the loop), whereas Figure 2(I.b) contains two field interactions on the bra (right branch). Track of time ordering is kept since TTS is a frequency-resolved signal, which requires the frequency-dispersed field to interact last with the molecule. In Figure 2(II), the interaction with the probe pulse is visualized as an absorption process, with one interaction on each branch of the loop. The diagrams in

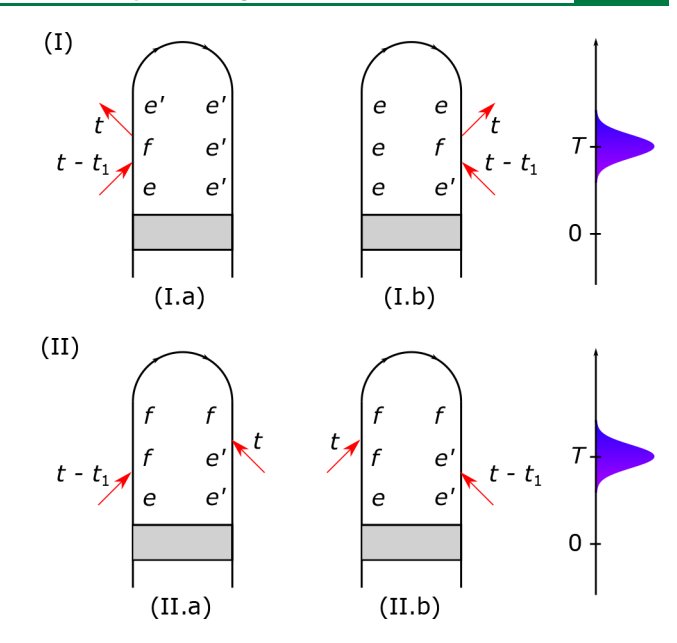


Figure 2. Equivalent loop diagrams representing the TTS signal. The shaded area represents the initial excitation of the molecule around t =0 and its subsequent nonadiabatic dynamics, resulting in a nonstationary superposition state $|\phi_e\rangle\langle\phi_{e'}|$, where e and e' label adiabatic electronic states. The probe pulse centered at T (purple pulse on the right) acts on the molecule at times $t - t_1$ and t, where both interaction times lie within the temporal envelope of the probe pulse. f denotes a core-excited state. The diagrams (I) and (II), summed over their respective (a) and (b) components, represent alternative, equivalent ways to visualize the same process and lead to the same expressions for the signal (eq 13), using the freedom to act with the dipole operators on the bra or the ket: (I) the probe acts twice (I.a) on the ket and (II.b) on the bra, inducing a Raman excitation between e and e' [see also Figure 1(I)]; (II) the probe is absorbed on the left and right branches [see also Figure 1(II)]. Since the TTS signal is dispersed in frequency, the frequency-dispersed field interacts last with the molecule, and track of time ordering is kept.

Figures 2(II.a) and 2(II.b) can be obtained from Figures 2(I.a) and 2(II.b), respectively, by moving the last interaction arrow along the loop. The diagrams of Figure 2(I) and Figure 2(II) are thus completely equivalent representations of the same process, using the freedom to act with the dipole operators on the bra or the ket. Figure 2(I) depicts TTS as a Raman process between states e and e' [see Figure 1(I)], while Figure 2(II) highlights the absorption of a photon from the e into the core f states [see Figure 1(II)].

Equation 13 is written in the adiabatic basis $\{|\phi_e\rangle\}$ of electronic space, and can be separated into contributions from the populations (e=e') and coherences $(e\neq e')$ in this basis. Note, however, that the exact separation of the TTS signal into population and coherence terms has to be performed in the exact basis of vibronic eigenstates in the joint electronic and nuclear space. These exact vibronic populations and coherences are independent of any basis set and are those we refer to hereafter.

3. X-RAY ATAS VS TRUECARS

We now show that ATAS and TRUECARS are special cases of TTS corresponding to different parameter regimes. When the probe pulse is resonant with the $e \rightarrow f$ transitions between valence and core states, $\omega_0 \approx \omega_{fv}$ the TTS signal in eq 13 is dominated by contributions from ground- and valence-state

populations and is referred to as transient absorption. Contributions from molecular coherences lead to modulations of the amplitudes of the spectral features, but these are typically weaker than those due to state populations. TRUECARS is instead an off-resonant TTS, which employs a probe pulse detuned from any transition energies in the molecule, ensuring a background-free detection of coherences.

3.1. Computation of the Resonant TTS Signal. For a molecule undergoing coupled nuclear and electronic dynamics, the resonant TTS signal of eq 13 can be computed exactly by introducing the core nuclear WPs

$$|\xi_{f}(t, t_{1})\rangle = \sum_{e} \hat{G}_{0,ff}(t, t - t_{1}) \hat{\mathbf{V}}_{fe}^{\dagger} \cdot \hat{\mathbf{e}} |\chi_{e}(t - t_{1})\rangle c_{e}(t - t_{1})$$

$$(15)$$

obtained by acting on $|\Psi(t-t_1)\rangle$ at $t-t_1$ with the dipole operator, and then letting the resulting core-excited WP propagate freely during t_1 . The signal then reads

$$S(\omega_{s}, T)$$

$$= -2\operatorname{Im}\left\{\tilde{\mathcal{E}}^{*}(\omega_{s} - \omega_{0}) \int dt \int_{0}^{\infty} dt_{1}\mathcal{E}(t - t_{1} - T) \right.$$

$$\times e^{i(\omega_{s} - \omega_{0})(t - t_{1} - T)} e^{i\omega_{s}t_{1}}$$

$$\times i \sum_{e'f} c_{e'}^{*}(t) \langle \chi_{e'}(t) | \hat{\mathbf{V}}_{e'f} \cdot \hat{\mathbf{e}} | \xi_{f}(t, t_{1}) \rangle \right\}$$

$$(16)$$

assuming that the WPs $|\xi_f(t, t_1)\rangle$ are known for each t and t_1 . Note that in Sec. 4, for our current simulations of the photodissociation of thiophenol, we will not treat explicitly the propagation of the nuclear WP on the core-excited PESs during t_1 , which is limited by the core lifetime, and will instead approximate the Green's function $\hat{G}_{0,ff}(t, t - t_1) \approx \mathrm{e}^{-\mathrm{i}\tilde{\omega}_f t_1} \mathrm{e}^{-\gamma_f t_1}$ locally at each point in nuclear space in terms of the core-state surfaces $\tilde{\omega}_t$.

3.2. Expressing Off-Resonant TTS in Terms of Electronic Polarizabilities. For an off-resonant X-ray probe, the core states f in Figure 1 are not populated, and the probe induces an instantaneous stimulated Raman process. This can be visualized by the diagrams of Figure 2, in the limiting case in which the system spends a very short time, $t_1 \rightarrow 0$, in the excited states f. For an off-resonant X-ray probe, the TTS signal (eq 13) can thus be recast in a more compact form in terms of the electronic polarizability. This is obtained by approximating the state in eq 15 as

$$|\xi_f(t, t_1)\rangle \approx \sum_e \hat{\mathbf{V}}_{fe}^{\dagger} \cdot \hat{\mathbf{e}} |\chi_e(t)\rangle c_e(t) e^{-i\tilde{\omega}_{fe}t_1}$$
(17)

where $\tilde{\omega}_{fe}$ is the transition energy between states f and e at a given point in nuclear space. By introducing the polarizability operator

$$\hat{\alpha}_{e'e} = i \sum_{f} \int_{0}^{\infty} dt_{1} e^{i(\omega_{0} - \tilde{\omega}_{fe})t_{1}} e^{-\epsilon t_{1}} \hat{\mathbf{V}}_{e'f} \cdot \hat{\mathbf{e}} \hat{\mathbf{V}}_{fe}^{\dagger} \cdot \hat{\mathbf{e}}$$

$$= -\sum_{f} \frac{\hat{\mathbf{V}}_{e'f} \cdot \hat{\mathbf{e}} \hat{\mathbf{V}}_{fe}^{\dagger} \cdot \hat{\mathbf{e}}}{\omega_{0} - \tilde{\omega}_{fe} + i\epsilon}$$
(18)

with the positive infinitesimal ϵ , the off-resonant TTS signal reads

$$S(\omega_{s}, T)$$

$$= -2\operatorname{Im}\left\{\tilde{\mathcal{E}}^{*}(\omega_{s} - \omega_{0}) \int dt \mathcal{E}(t - T) \times e^{i(\omega_{s} - \omega_{0})(t - T)} \sum_{ee'} c_{e'}^{*}(t) c_{e}(t) \langle \chi_{e'}(t) | \hat{\alpha}_{e'e} | \chi_{e}(t) \rangle \right\}$$
(19)

This same equation could be alternatively derived by using the effective light-matter interaction Hamiltonian $\hat{H}_{\text{int}} = -\hat{\alpha}\hat{\mathbf{E}}^{\dagger}\cdot\hat{\mathbf{E}}$. In Sec. S1 in the SI, we show how the polarizability operator $\hat{\alpha}$ in eq 18 can be expressed in terms of charge- and current-density operators when using the minimal-coupling Hamiltonian.

The off-resonant TTS signal in eq 19 is expressed in terms of a polarizability operator which directly couples the molecular ground and valence states. This results from the fact that an off-resonant X-ray probe does not induce any core-state dynamics contributing to the signal. We stress, however, that the ground/valence state dynamics induced by an X-ray probe pulse off resonant from the molecular f-e transitions significantly differ from those that would be induced by a UV/vis probe pulse resonant with the e-e' transitions. First, an attosecond X-ray probe provides the short duration and broad bandwidth required to simultaneously monitor a broad superposition of e states with high temporal resolution, while a UV/vis probe would selectively probe given e-e' transitions with a resolution determined by the longer UV/vis pulse duration. Second, off-resonant X-ray TTS provides direct access to the e-e' coherences, as discussed in the following, whereas the transient absorption signal of a resonant UV/vis pulse would still be dominated by population contributions. Hereafter, we thus compare TTS for an X-ray pulse either resonant or off resonant to the core states in the molecule.

3.3. Resonant vs Off-Resonant TTS. 3.3.1. Key Features for a Few-Electronic-Level Model. To highlight the key differences between resonant and off-resonant TTS, we start by considering a few-level model where, for the moment, we neglect nuclear dynamics or nonadiabatic effects and focus on how adiabatic electronic populations and coherences are encoded in the signals. We assume a few-level system in a coherent superposition of ground/valence states, $|\Psi(t)\rangle = \sum_e c_e \mathrm{e}^{-\mathrm{i}\omega_e t}|e\rangle$, and a resonant TTS experiment in which the X-ray probe couples each state $|e\rangle$ to the higher-frequency state $|f\rangle$, with propagator $G(t, t - t_1) = \mathrm{e}^{-\mathrm{i}\omega_p t_1}\mathrm{e}^{-\gamma_p t_1}$, transition couplings V_{fe} state frequencies ω_e and ω_p and the decay rate γ_f of the excited state $|f\rangle$. Under these conditions, the population $(\rho_{ee} = |c_e|^2)$ and coherence $(\rho_{e'e}(T) = c_e c_e^* \mathrm{e}^{-\mathrm{i}\omega_{e'e}T})$ contributions to the ATAS signal are given by

$$S_{\text{res,pop}}(\omega_{s}, T)$$

$$= -2\sum_{e} \frac{\gamma_{f}}{(\omega_{s} - \omega_{fe})^{2} + \gamma_{f}^{2}} |\tilde{\mathcal{E}}(\omega_{s} - \omega_{0})|^{2} |V_{fe}|^{2} \rho_{ee}$$
(20)

and

$$S_{\rm res.coh}(\omega_{\rm s}, T)$$

$$= -2\operatorname{Im}\left\{\sum_{e} \frac{\gamma_{f} + i(\omega_{s} - \omega_{0})}{(\omega_{s} - \omega_{fe})^{2} + \gamma_{f}^{2}} \tilde{\mathcal{E}}^{*}(\omega_{s} - \omega_{0})\right\}$$

$$\times \sum_{e' \neq e} \tilde{\mathcal{E}}(\omega_{s} - \omega_{0} - \omega_{e'e}) V_{ef} V_{fe'} \rho_{e'e}(T)$$

respectively. The above expressions show that the ATAS spectrum contains peaks at the transition energies ω_{f_e} between the core and the ground/valence states in the system. This is indicative of the fact that a real photon is absorbed in the resonant excitation of the core state. The contribution from the populations features Lorentzian lines centered at ω_{tv} of width γ_{θ} and with a strength determined by the pulse spectral intensity $|\tilde{\mathcal{E}}(\omega_s - \omega_0)|^2$, the dipole coupling $|V_{fe}|^2$, and the population ρ_{ee} . The contribution from the coherences gives rise to lines whose shapes are determined by the phase of $\rho_{e'e}(T)$, varying periodically with T from a symmetric, Lorentzian to an asymmetric, Fano-like line shape. The coherence contribution $S_{\rm res,coh}(\omega_{\rm s}, T)$ involves a resonant Raman excitation $e' \to f \to e$ via the core state $|f\rangle$. Its strength is therefore determined by the spectral amplitude of the probe pulse at two frequencies, $\mathcal{E}(\omega_{\rm s}-\omega_0)$ and $\mathcal{E}(\omega_{\rm s}-\omega_0-\omega_{e'e})$, separated by $\omega_{e'e}$; and by the two dipole couplings $V_{\it ef}$ and $V_{\it fe'}$ involved in the Raman

If an off-resonant X-ray probe pulse is used, the TTS signal probing the superposition state $|\Psi(t)\rangle = \sum_e c_e e^{-i\omega_e t} |e\rangle$ reads

$$\begin{split} S_{\text{off-res}}(\omega_{s}, T) \\ &= -2\text{Im} \Biggl\{ \sum_{e} \sum_{e' \neq e} \tilde{\mathcal{E}}^{*}(\omega_{s} - \omega_{0}) \tilde{\mathcal{E}}(\omega_{s} - \omega_{0} - \omega_{e'e}) \\ &\times \alpha_{ee'} \rho_{e'e}(T) \Biggr\} \end{split}$$

$$(22)$$

Population contributions are completely absent in the offresonant TTS signal, because the argument in eq 22 is real when e=e', and the signal does not carry any contribution from ρ_{ee} . As a result, the TTS signal with an off-resonant probe provides direct, background-free access to the coherences. Recasting the off-resonant TTS signal in terms of the Raman frequency $\omega_R = \omega_S - \omega_{00}$

$$S_{\text{off-res}}(\omega_{R}, T)$$

$$= -2\text{Im} \left\{ \sum_{e} \sum_{e' \neq e} \tilde{\mathcal{E}}^{*}(\omega_{R}) \tilde{\mathcal{E}}(\omega_{R} - \omega_{e'e}) \alpha_{ee'} \rho_{e'e}(T) \right\}$$
(23)

also reveals that the off-resonant TTS signal is given by a redistribution of gain and loss within the frequency width of the probe pulse. Absorption at positive Raman frequencies is always accompanied by emission at negative Raman frequencies and vice versa, and the number of photons is conserved. This is in contrast to the resonant setup used in ATAS, where real photons are absorbed and their number is therefore not conserved.

3.3.2. Resonant vs Off-Resonant TTS for Nonadiabatic Dynamics. For molecules undergoing nonadiabatic dynamics, the above-discussed separation into population and coherence

contributions has to be performed in the exact basis of vibronic eigenstates in the joint electronic and nuclear space. ATAS is typically dominated by strong contributions from vibronic populations. These terms do provide information about the NAP and are imprinted in ATAS as the transient appearance or splitting of absorption lines. ^{27–31,34} However, state populations are always present, and are therefore less indicative of nonadiabatic dynamics than the coherences, which only emerge as a result of the NAP itself. Although vibronic coherences do contribute to the ATAS signal, they often remain hidden underneath the larger population contribution. In off-resonant TTS, coherences are instead the only terms contributing to the signal, providing direct access to NAPs.

- **3.4. TRUECARS.** TRUECARS represents a particular case of off-resonant TTS that specifically aims at probing the molecular coherences created in a NAP.¹⁷ The TTS signal reduces to TRUECARS when the two following conditions are met:
 - 1. the probe is off-resonant;
 - 2. the pump does not generate a coherence between the electronic states involved in the NAP.

Under these conditions, it is possible to unambiguously recognize the transient changes in the transmission spectrum that are due to the coherences generated during the NAP. The photon number does not change by the interaction with matter, and only shows a redistribution of gain and loss in the spectrum of the transmitted probe resulting from inelastic scattering off coherences. Elastic scattering from populations does not lead to any absorption of the X-ray probe pulse, and therefore the TRUECARS signal contains no signatures from populations. Note that the pump pulse may generate coherences between other states. However, if these states are not involved in the NAP, the coherence contributions initially created by the pump can be distinguished from the coherences created at the NAP thanks to the frequency resolution of TRUECARS. This will be clearly illustrated by our simulations of the TRUECARS signal monitoring the photodissociation of thiophenol in the following section.

To enhance the joint spectral/temporal resolution, the original TRUECARS proposal 17 had employed a hybrid broad- $\tilde{\mathcal{E}}_{\rm B}(\omega-\omega_{\rm B0})$ and narrowband $\tilde{\mathcal{E}}_{\rm N}(\omega-\omega_{\rm N0})$ X-ray probe pulse, with central frequencies $\omega_{\rm B0}$ and $\omega_{\rm N0}$, respectively. 17 The signal is obtained by measuring the frequency-dispersed transmitted broadband pulse $\tilde{\mathcal{E}}_{\rm B}(\omega-\omega_{\rm B0})$,

$$S(\omega_{s}, T)$$

$$= -2\operatorname{Im}\left\{\tilde{\mathcal{E}}_{B}^{*}(\omega_{s} - \omega_{B0}) \int dt \mathcal{E}_{N}(t - T) \times e^{i(\omega_{s} - \omega_{N0})(t - T)} \sum_{ee'} c_{e'}^{*}(t) c_{e}(t) \langle \chi_{e'}(t) | \hat{\alpha}_{e'e} | \chi_{e}(t) \rangle \right\}$$
(24)

The broadband component $\tilde{\mathcal{E}}_{\rm B}(\omega-\omega_{\rm B0})$ now provides a broad spectral observation window to cover the range of transition energies spanned during the NAP and ensures attosecond temporal resolution, while the narrowband pulse $\tilde{\mathcal{E}}_{\rm N}(\omega-\omega_{\rm N0})$ provides a reference for the frequency resolution of the technique. It was later pointed out that stochastic probe pulses from, e.g., free-electron lasers may also be used to achieve joint high temporal and spectral resolutions, by using a covariance detection. ¹⁹ In that case, the broad

average spectral envelope of the stochastic pulse plays the role of $\tilde{\mathcal{E}}_{\rm B}(\omega-\omega_{\rm B0})$, while the role of $\mathcal{E}_{\rm N}(t)$ is played by its long average temporal envelope.

4. PROBING NONADIABATIC PASSAGES IN THE PHOTODISSOCIATION OF THIOPHENOL

We now apply TRUECARS and ATAS to probe two nonadiabatic transitions in the photodissociation of the S-H bond in thiophenol. This is a prototypical system for investigations of kinetic isotope effects upon UV-induced photodissociation of heteroaromatic molecules. 42 In earlier studies on thiophenol, the S-H distance and S-H torsion have been identified as the tuning and coupling mode of the CI.^{43–46} These lift the degeneracy between the electronic states, facilitating the nonadiabatic transition through CIs. Our effective Hamiltonian uses the C-S-H angle instead of the S-H torsion as the second reactive nuclear coordinate. 4/ This results in not capturing the conical shape of the electronic state intersection, but the coupling seam rather spans along the C-S-H angle for a fixed S-H distance (see Figure S2 in the SI). This is a common side effect of choosing reactive nuclear degrees of freedom, where the chosen coordinates do not necessarily feature exactly the two coordinates lifting the energetic degeneracy and forming the CI, but instead map a certain section of the coupling space spanned by the remaining 3N - 8 degrees of freedom, also called the CI seam. Thus, we hereafter use the term "nonadiabatic passage" instead of "conical intersection". Our model Hamiltonian may lead to shorter relaxation times than exact models. 48,49 It also misses the geometric phase experienced by a molecular WP encircling a CI, which is anyway not captured by the TTS signal. All properties of the TTS signal discussed here straightforwardly apply to any kind of NAP.

Two-dimensional adiabatic PESs of the three valence electronic states are depicted in Figure S2 in the SI. These were calculated with ab initio electronic structure methods (see details in Appendix A). Ten Sulfur L_1 edge core excited states were computed for the ATAS signal by the same protocol. Two NAPs along the S–H distance (the first coordinate), NAP-1 (between S_2 and S_1 near 1.5 Å) and NAP-2 (between S_1 and S_0 near 2.7 Å), provide an efficient relaxation and dissociation channel for photoexcited thiophenol (Figure 3). $^{50-52}$

Quantum dynamical simulations in the reduced twodimensional nuclear space were performed by numerically solving the time-dependent Schrödinger equation on the adiabatic PESs including nonadiabatic couplings, allowing for a fully quantum mechanical treatment of both electrons and nuclei in the NAP (see details in Appendix B). A 20 fs full width at half-maximum (fwhm) optical pump, in resonance with the S₀ to S₁ transition, initially prepares a part of the nuclear WP in the S₁ state. The S₁ WP tunnels to NAP-1 within 10 fs, creating a vibronic coherence between S₁ and S₂ [see Figure S3(a) in the SI]. Due to the large kinetic energy acquired in the strongly repulsive potential, the WP reaches the NAP-2 within T = 20 fs. Note, however, that the vibronic coherence created at NAP-2 is masked by the one created by the optical pump pulse. In the impulsive excitation limit, the S_0/S_1 coherence created at NAP-2 is well resolved [see Figure S3(b) in the SI]. We apply a Butterworth filter⁵³ in order to prevent artificial back-evolution of the parts of the WP which reach the dissociation limit at 10 Å.

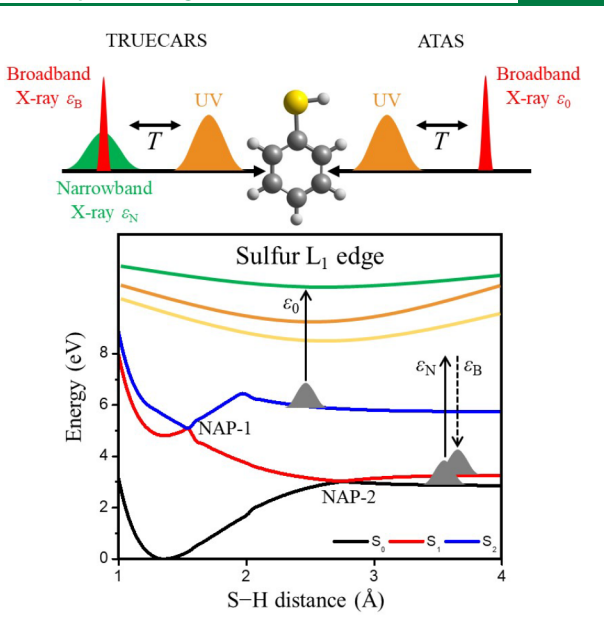


Figure 3. TRUECARS and ATAS of thiophenol photodissociation. (top) Pulse configuration of (left) TRUECARS and (right) ATAS exciting the thiophenol molecule shown in the center. (bottom) Level scheme and induced dynamics. A 20 fs UV pulse excites the molecule into the S_1 state (red), which is followed by a passage through NAP-1 between S_1 and S_2 (blue) and a passage through NAP-2 between S_1 and S_0 (black). In TRUECARS, a hybrid femtosecond narrowband $\mathcal{E}_{\rm N}$ /attosecond broadband $\mathcal{E}_{\rm B}$ off-resonant pulse probes the nonadiabatic dynamics at time delay T. In ATAS, this is achieved by a single broadband \mathcal{E}_0 probe resonant to the sulfur core states at the L_1 edge (green, orange, yellow) in the molecule.

The pump, probe, and molecular parameters required to compute the TRUECARS and ATAS signals are summarized in Table 1. For calculating the TRUECARS signal (eq 24), we assume a phase-matched, hybrid probe consisting of a $\tilde{\mathcal{E}}_{\rm B}^*(\omega_{\rm s}-\omega_{\rm 0})$ broadband (500 as) and a $\mathcal{E}_{\rm N}(t-T)$ narrowband (2 fs) X-ray pulse, both centered at ω_0 = 200 eV. For ATAS (eq 13), we use a single broadband (20 eV) pulse, $\tilde{\mathcal{E}}_0^*(\omega_s - \omega_0)$, with central frequency $\omega_0 = 230$ eV. We approximate the Green's function $\hat{G}_{0,ff}(t,\,t-t_1) pprox {
m e}^{-{
m i}\tilde{\omega}_f t_1} {
m e}^{-\gamma_f t_1}$ locally at every point in nuclear space and set the core-state widths to $\gamma_f = 1.34$ eV.⁵⁴ Note that the transition energies, transition dipole moments, and thus the electronic polarizabilities (eq 18) are functions of the nuclear coordinates R. The geometry-dependent $\omega_{fe}(\mathbf{R})$, $V_{e'f}(\mathbf{R})$, $\alpha_{e'e}(\mathbf{R})$, and the nuclear overlap $\chi_{e'}(\mathbf{R}, t)\chi_{e}(\mathbf{R}, t - t_1)$ were all evaluated on a 1024 × 256 numerical grid. For the calculation of the TRUECARS and ATAS signals, these functions are correspondingly integrated in nuclear space, including the time dependence of the electronic coefficients $c_{e'}(t)c_e(t-t_1)$ and nuclear overlap $\chi_{e'}(\mathbf{R}, t)\chi_{e}(\mathbf{R}, t - t_1)$ obtained by solving the Schrödinger equation.

The calculated TRUECARS signal is displayed in Figure 4(a). A frequency window between -2 and 2 eV is used in order to selectively detect the vibronic coherences crated at the NAP. Additional contributions due to the coherences created by the pump appear at larger Raman frequencies. This is apparent in Figure S4 in the SI, where we show the TRUECARS signal in a broader frequency window and the TRUECARS signal in the impulsive limit. Observing TRUECARS at the relevant Raman frequencies thus enables

Table 1. Pulse and Molecular Parameters for TRUECARS and ATAS Signals

Technique	Signal Expression	Pump pulse fwhm (central frequency)	Probe pulse fwhm (central frequency)	Molecular parameters
TRUECARS	eq 24	20 fs	2 fs $\mathcal{E}_{\mathrm{N}}/500$ as \mathcal{E}_{B}	$\alpha_{ee'}(\mathbf{R})$, eq 18
		$(\omega_{\rm pu} = 4.81 \text{ eV})$	$(\omega_{\rm N0} = \omega_{\rm B0} = 200 \text{ eV, Off-resonant})$	
ATAS	eq 13	20 fs	20 eV \mathcal{E}_0	$\gamma_f = 1.34 \text{ eV}$
		$(\omega_{\rm pu} = 4.81 \text{ eV})$	$(\omega_0 = 230 \text{ eV, Resonant})$	$V_{e'f}\!(R),\;\omega_{fe}\!(R)$

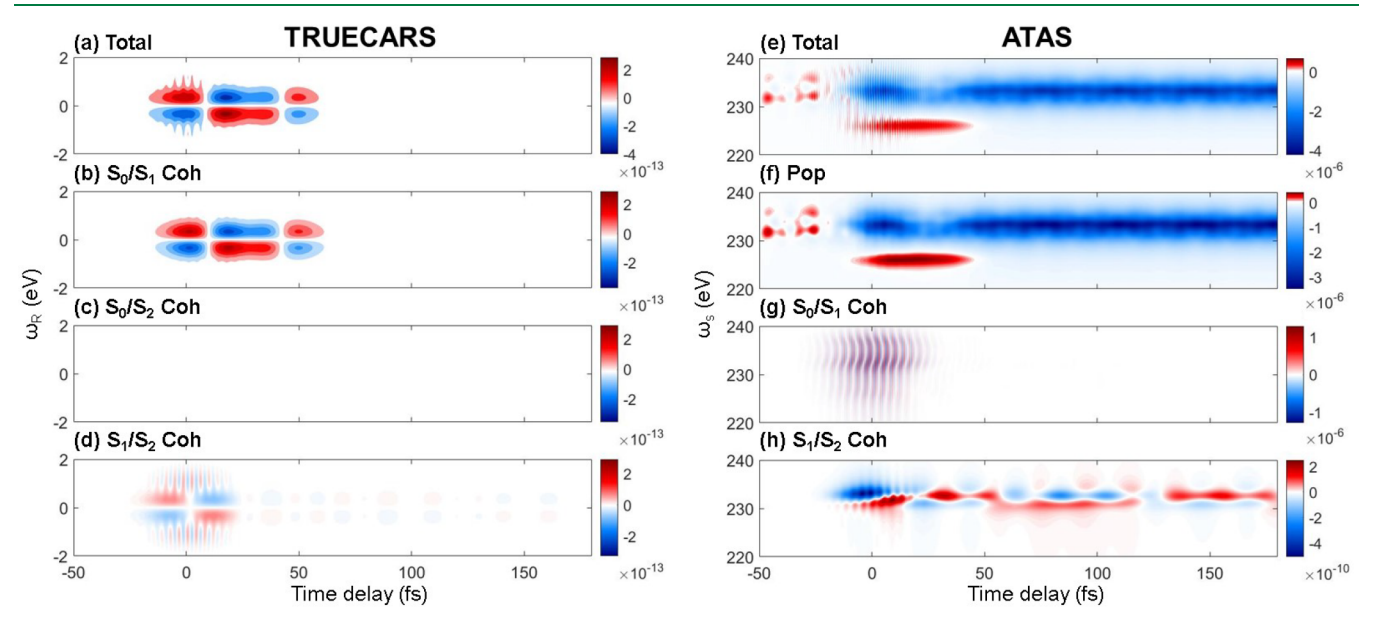


Figure 4. Comparison of the TRUECARS and ATAS signals. (left) The (a) total TRUECARS signal and contributions from (b) S_0/S_1 , (c) S_0/S_2 , and (d) S_1/S_2 coherences are separately plotted. (right) The (e) total ATAS signal and contributions from (f) population, (g) S_0/S_1 coherence, and (h) S_1/S_2 coherence to the total ATAS signal are also shown. The ATAS signal is here plotted as a difference spectrum, after subtracting the ground state absorption spectrum in the absence of the UV pump pulse from the time-dependent absorption spectrum.

one to isolate coherence contributions created at CIs/ACs. We first note that the signal directly monitors the coherences generated at the NAP with no contributions from populations. The signal appears at around $\omega_R = 0$ eV, reflecting the degeneracy of the involved electronic states during the NAP. The different contributions from coherences, S_0/S_1 , S_0/S_2 , and S₁/S₂, to the signal are separately plotted in Figures 4(b)-4(d). For our 20 fs UV pump, the S_1/S_2 coherence first appears at around -10 fs [Figure 4(d)], followed by a delayed contribution of S_0/S_1 at around 0 fs [Figure 4(b)]. This matches the evolution of the WP discussed above. The S₂ WP oscillates within the adiabatic potential well (between 1.4 and 1.6 Å) passing by NAP-1 continuously, hence the signal is visible throughout the entire propagation time. By the same argument, the finite nuclear WP overlap with the S₁ WP near the Franck-Condon point shows up in the signal at $\omega_{\rm R} \simeq 1.0$ eV as a fast-oscillating feature [Figure 4(d)]. The strength of the TRUECARS signal is directly proportional to the amplitude of the coherences generated at the NAP. While the amplitude of these coherences can be low [see, e.g., Figure 4(a)] it can be increased and maximized, e.g., by using a quantum-controlled pump pulse. 55

These coherence signatures are masked in the ATAS signal by the stronger population contributions, as shown in Figure 4(e). Here, we display difference spectra, obtained after subtracting the ground state absorption spectrum in the absence of the UV pump pulse from the time-dependent ATAS signal. The contributions from electronic population, S_0/S_1 , and S_1/S_2 coherences are plotted in Figures 4(f)-4(h). The

total signal appears to be dominated by photoinduced absorption from transiently populated valence excited states, with an increase or decrease in the signal in response to the electronic dynamics [Figure 4(f)]. We also observe oscillatory features at around $\omega_s = 232$ eV and $T \simeq 0$ fs, due to the S_0/S_1 coherences created by the UV pump pulse [Figure 4(g)]. The coherence created by the NAP is 4 orders of magnitude smaller, hence masked in the ATAS signal [Figure 4(h)]. We observe a slower temporal oscillation and narrower spectral width of the S_1/S_2 signature than for the S_0/S_1 coherence, indicating the smaller transition energy between the states involved in the NAP.

The ATAS signal has two main peaks at around 226 and 232 eV [Figure 4(e)]. The lower one represents a pre-edge peak where the sulfur 2s electron is promoted to a semivacant π valence orbital. After NAP-1, the S_1 state is mainly characterized by ${}^1\pi\sigma^*$, S_2 by ${}^1\pi\pi^*$, and C_1 by the $2s \to \sigma^*$ configuration. The σ^* orbital has a pronounced molecular-orbital coefficient on the sulfur atom, whereas the π^* orbital does not. Hence, the sulfur 2s to π^* transition is prohibited and only S_1 contributes to the pre-edge peak. In contrast, the higher peaks observed at around 232 to 233 eV overlap with the ground state bleach signature, where the sulfur 2s electron is promoted to the σ^* orbital (ground state to C_1 transition).

ATAS indirectly probes the NAP through the evolution of absorption peaks, such as the bifurcation or the appearance of new peaks. ^{29,30,56} This is caused by the nuclear WP, initially located in a single electronic state, bifurcating at the NAP and generating new absorption lines. These may evolve independ-

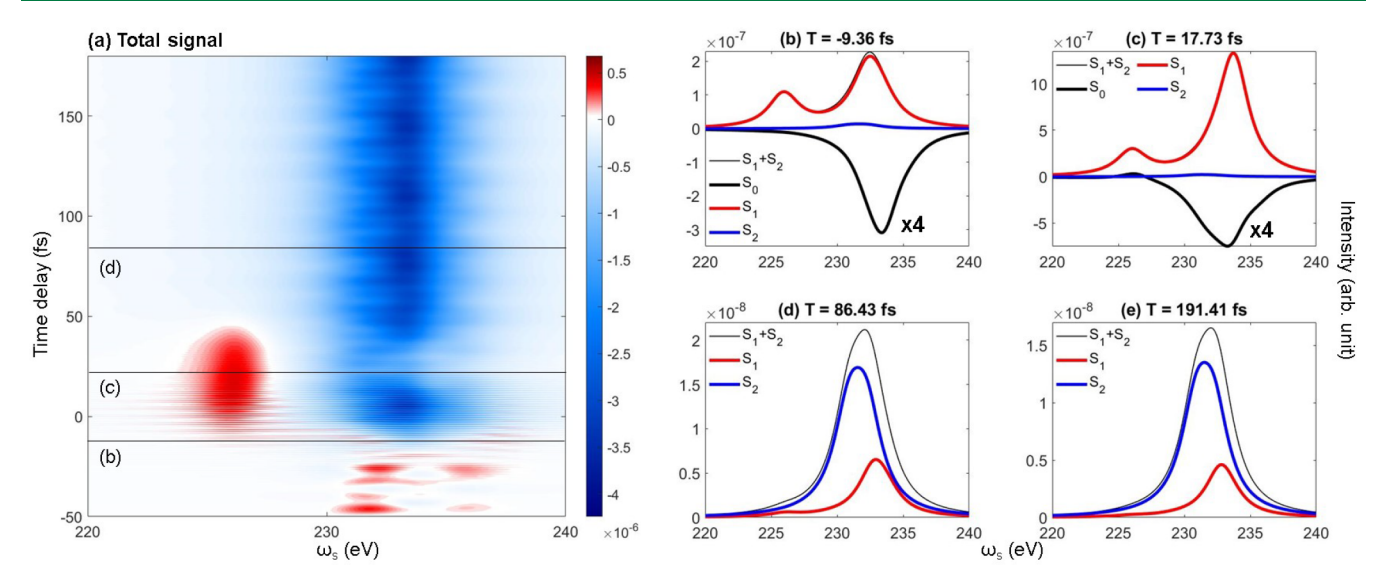


Figure 5. Probing thiophenol photodissociation dynamics by ATAS. (a) Total ATAS signal as in Figure 4(e), where the color is rescaled to emphasize the excited state absorption signatures. (b)–(e) Traces of the signal at time delays (b) T = -9.36 fs, (c) T = 17.73 fs, (d) T = 86.43 fs, and (e) T = 191.41 fs. The ground state bleach (S_0) is rescaled by a factor 0.25 in panels (b) and (c) and is not displayed in panels (d) and (e) to emphasize the signatures from the S_1 and S_2 absorption peaks.

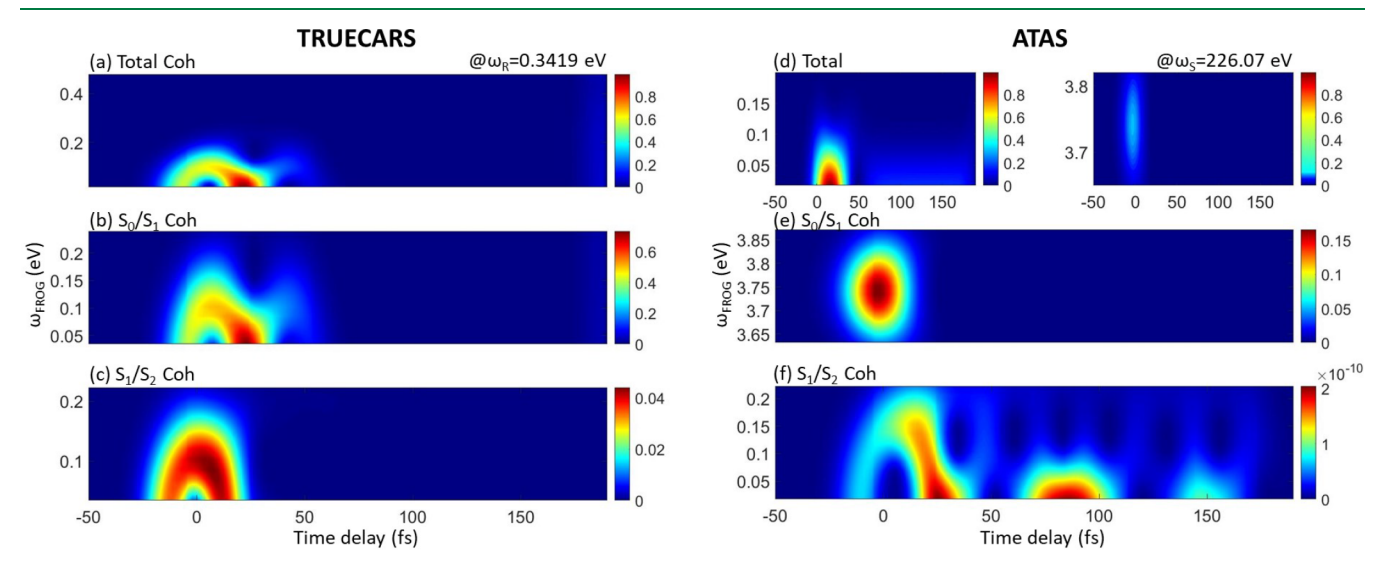


Figure 6. FROG spectrograms of the TRUECARS and ATAS signals. The spectrograms (eq 25) are extracted (a)–(c) from the TRUECARS signal at a Raman frequency of $\omega_R = 0.3419$ eV, and (d)–(f) from the ATAS signal at a detection frequency of $\omega_s = 226.07$ eV. The total spectrogram at $\omega_s = 226.07$ eV in panel (d) is dissected into two different ω_{FROG} windows to emphasize two different features at 0.05 and 3.72 eV.

ently thereafter due to different gradients in the electronic PESs of the valence states. We track the evolution (kinetics) of the spectral lines at a given pump-probe time delay T as shown in Figure 5. At T = -9.36 fs, the S₁ state is populated by the pump, and its spectroscopic signatures appear at 226 and 232 eV [Figure 5(b)]. As the nuclear WP reaches NAP-1, the S₂ absorption line appears at around 231.78 eV, which overlaps with the ground state bleach. At T = 17.73 fs, the excited state absorption feature becomes strongest [Figure 5(c)]. The preedge peak vanishes after 86.43 fs, and the excited state absorption from S₂ appears at 231.73 eV, while that from S₁ appears at 233.78 eV [Figures 5(d) and 5(e)]. We note that the S₁ and S₂ signatures overlap throughout the entire propagation time due to the large broadening of the S 2s edge. The large lifetime broadening of the core states, as in our thiophenol L₁ edge case, can therefore represent a limit for time-resolved ATAS studies, as it can prevent the detection of absorption-line splitting. This is also exemplified in Figure S5 in the SI, where we display the ATAS signal in the impulsive excitation limit with a narrower lifetime width, $\gamma_f = 0.134$ eV.

An alternative way to retrieve coherence information is by spectrograms obtained by postprocessing of the ATAS signal. As shown in Figures 4(c) and 4(d), the coherence contribution features time-dependent oscillations at regions around the transition energy of the involved vibronic states. We visualize the dynamical evolution of this frequency by convolving the trace of the signal (TRUECARS or ATAS) S(t), evaluated at a particular frequency (ω_R or ω_s , respectively), with a Gaussian gating function $E_{\text{gate}}(t)$ with 0.48 fs fwhm, scanning the trace at each time delay T_{coh} , similar to a frequency-resolved optical-gating (FROG) measurement: ⁵⁷

$$I_{\text{FROG}}(\omega_{\text{FROG}}, T_{\text{FROG}})$$

$$= \left| \int_{-\infty}^{\infty} dt S(t) E_{\text{gate}}(t - T_{\text{FROG}}) e^{-i\omega_{\text{FROG}} t} \right|^{2}$$
(25)

The resulting spectrogram of the signal trace S(t) reveals the energy splitting ω_{FROG} of the involved state at each time delay.

The FROG spectrograms of the TRUECARS and ATAS signals are compared in Figure 6. The TRUECARS spectrogram at ω_R = 0.3419 eV directly reveals the timing and the energy splitting during the NAPs, where the signatures from the S_1/S_2 coherence appear first, followed by those stemming from the S_0/S_1 coherence. Due to the electronic degeneracy during the NAP, the spectrogram appears at around 0.05 eV. The ATAS spectrogram shown in Figure 6(d) (for ω_s = 226.07 eV) exhibits two components at different $\omega_{ ext{FROG}}$ frequencies, one at around 0.05 eV and another one at around 3.72 eV. We find that the slowly varying signature at 0.05 eV comes from the populations, and the latter one from the S_0/S_1 coherence created by the pump [Figure 6(e)]. The spectrogram of the S_1/S_2 coherence [Figure 6(f)] offers similar information to the TRUECARS spectrogram [Figure 6(c)], but is 10 orders of magnitude weaker than the populations. Thus, its signature in Figure 6(d) is buried.

5. DISCUSSION AND CONCLUSIONS

Our theoretical study shows that TRUECARS and ATAS are the off-resonant- and resonant-probe limits of the same timeresolved transmission spectroscopy technique.

TRUECARS directly probes the emergence of coherences in a background-free manner. By observing the signal at various Raman shifts, different coherence contributions can be directly distinguished. This allows one to isolate the coherence contributions emerging at NAPs such as CIs or ACs, and follow them in a time-resolved manner. The evolution of the WP in different PESs is encoded both in the Raman shift ω_R at which the absorption signal is centered, as well as in the modulation of the signal with time delay. TRUECARS does not require a postprocessing analysis based on FROG spectrograms in order to highlight coherence contributions, since background population terms are absent. The signal strength can be low due to the small amplitude of the coherences generated at the NAP, but quantum-control techniques can be employed to suitably shape the pump pulse and maximize the signal strength.⁵³

ATAS, in contrast, is dominated by population terms. This allows one to track the evolution of the electronic states with the unique advantages of XUV and X-ray sources, such as excellent temporal resolution and sensitivity to optically dark valence states due to different selection rules of core-excited states. A0,58 At the same time, we have shown that the weaker modulations in the signal due to the coherences can be highlighted in ATAS, e.g., by computing a FROG spectrogram.

Comparing the FROG spectrograms of ATAS and TRUECARS offers a more direct comparison of how the two techniques access molecular coherences. We find that the S_1/S_2 vibronic coherence is similarly extracted by the spectrograms of both signals. This implies that the TRUECARS signal can access the coherence information from the total signal independent of core-to-valence selectivity. In contrast, the amplitude of the ATAS features does depend on core-to-valence couplings. Tuning the X-ray probe to different core states can thus provide additional information

about the couplings between different valence and core states in molecules.

Our simulations of the TRUECARS signal assumed a perfectly phase-matched hybrid pulse, with the broadband component ensuring a broad spectral observation window and good temporal resolution, and the narrowband pulse providing a reference for the frequency resolution. Although this precise phase control between two pulses represents a major difficulty in the implementation of TRUECARS with existing stochastic pulses from free-electron lasers, this obstacle could be overcome by implementing a correlation analysis of TRUECARS signals obtained with a single stochastic probe pulse. ¹⁹

The TTS signal by nature does not capture topological effects of CIs. It rather monitors the populations and coherences during nonadiabatic molecular photochemistry, and applies to any kind of nonadiabatic transition between electronic states, which we exemplify for S-H photodissociation here. Our work has connected ATAS and TRUECARS within the same TTS formalism. Future work could investigate the connection between TTS, which involves the absorption of a resonant (ATAS) or off-resonant (TRUECARS) probe, and X-ray emission spectroscopy. ¹⁰

With advances in the generation of XUV and X-ray attosecond pulses, the direct observation of nonadiabatic dynamics enabled by TRUECARS and ATAS will become a valuable tool to decipher and control the time-scale and outcomes of photophysical and photochemical reactions. We showed that the Raman excitation involved in TRUECARS and the absorption process determining ATAS are actually two ways of understanding the same process. By introducing a general TTS formalism, we establish the deep connection between the two techniques, which will benefit current and future experimental studies of time-resolved X-ray absorption spectroscopy, and enable extensions toward new parameter regimes.

APPENDIX A. QUANTUM CHEMISTRY

The computation of the PESs for the valence adiabatic states is described in ref 52. This was performed at the complete active space self-consistent field (CASSCF) level, by employing an active space of 12 electrons in 11 orbitals following ref 47 (including three pairs of π/π^* orbitals of the benzene ring, a nonbonding p-orbital of sulfur, and $\sigma_{S-H}^{(*)}$, and $\sigma_{C-S}^{(*)}$ orbitals) and a 6-311++G(d,p) basis set. The nonadiabatic coupling matrix elements of S_2/S_1 and S_1/S_0 were calculated at the same level of theory, by displacing the molecular structure along the two reactive coordinates. In the present study, a larger (14/12)active space was used to calculate the 10 lowest core excited states by rotating the sulfur 2s orbital into active space. The valence and ground states were recomputed with the same protocol to evaluate the valence-core transition dipole moments $V_{e'f}$. The electronic polarizabilities $lpha_{e'e}$ were calculated using eq 18 for an X-ray probe off-resonant (ω_0 = 200 eV) to the 10 lowest sulfur 2s core-excited states. Note that the transition energies, valence-core transition dipole moments, and thereby the polarizabilities are functions of the nuclear coordinates R. All quantum chemical calculations were performed with MOLPRO.59

APPENDIX B. WAVEPACKET SIMULATIONS

The photoinduced S–H bond dissociation in thiophenol was simulated using exact quantum nuclear WPs⁶⁰ in a reduced two-dimensional space spanned by the two nuclear degrees of freedom. The first coordinate corresponds to the S–H bond distance, the second to the H–S–C angle.⁴⁷ PESs and molecular quantities required for WP simulations and X-ray signal computations such as, e.g., nonadiabatic couplings and transition dipole moments in this two-dimensional space were calculated with ab initio quantum chemistry and subsequently discretized on a numerical grid with 1024 grid points in S–H and 256 grid points in H–S–C. The effective Hamiltonian is given by

$$H_{ee} = T + V_e(R) \tag{26}$$

$$H_{ee'} = K_{ee'} - V_{ee'} \mathcal{E}_{pu}(t) \tag{27}$$

where T is the kinetic energy operator, given in the G-Matrix formalism, 61 according to

$$T \simeq -\frac{\hbar^2}{2m} \sum_{o=1}^2 \sum_{p=1}^2 \frac{\partial}{\partial q_o} \left[G_{op} \frac{\partial}{\partial q_p} \right]$$
 (28)

with $o, p \in R$ and the G-Matrix computed via its inverse elements

$$(G^{-1})_{op} = \sum_{i=1}^{3N} m_i \frac{\partial x_i}{\partial q_o} \frac{\partial x_i}{\partial q_p}$$
(29)

 $K_{ee'}$ approximate the nonadiabatic couplings between the electronic states e and e', and is given by

$$K_{ee'} = \frac{1}{2m} \left(2f_{ee'} \frac{\partial}{\partial \mathbf{R}} + \frac{\partial}{\partial \mathbf{R}} f_{ee'} \right)$$
(30)

with $f_{ee'}$ containing terms $\left\langle \phi_e \middle| \frac{\partial}{\partial R} \phi_{e'} \right\rangle$ with the electronic wave function φ . The electronic coupling between S_0 and S_2 is neglected since there is no transition between them. The magnitude of electronic coherences affected by geometric phase effects is currently under debate, ⁶² which may influence the relative magnitudes of population and coherence terms in the discussed signals. The nuclear dynamics were launched by using a 20 fs fwhm Gaussian laser pump in resonance with the $S_0 \rightarrow S_1$ transition,

$$\mathcal{E}_{pu}(t) = a_{pu}e^{-(t-t_0)^2/2\sigma^2}\cos(\omega_{pu}(t-t_0))$$
(31)

where $a_{\rm pu}=1.5\times 10^{-2}$ a.u. is the electric-field amplitude, corresponding to a total intensity of 7.896 \times 10¹² W/cm². $\omega_{\rm pu}=4.81$ eV is the central frequency corresponding to the energy gap between the ground state and the S₁ state at the Franck–Condon point, and $\sigma=20$ fs is the temporal duration of the pump pulse. The nuclear WP is propagated by numerically solving the time-dependent Schrödinger equation on a two-dimensional nuclear grid with Chebychev⁶³ scheme using a 0.05 fs time step until 190 fs. A Butterworth filter⁵³ absorbs the part of WP reaching a distance of S–H 10 Å in all three valence states.

ASSOCIATED CONTENT

Supporting Information

The Supporting Information is available free of charge at https://pubs.acs.org/doi/10.1021/acs.jctc.3c00062.

A derivation of the TTS signal using the minimal coupling Hamiltonian; a comparison of the loop vs ladder diagram representations of the TTS signal; and additional simulation results in thiophenol (PDF)

AUTHOR INFORMATION

Corresponding Authors

Stefano M. Cavaletto — Department of Chemistry and Department of Physics & Astronomy, University of California Irvine, Irvine, California 92697, United States; oorcid.org/0000-0003-1516-7519; Email: smcavaletto@gmail.com

Yeonsig Nam – Department of Chemistry and Department of Physics & Astronomy, University of California Irvine, Irvine, California 92697, United States; ⊚ orcid.org/0000-0003-0386-9118; Email: yeonsign@uci.edu

Shaul Mukamel — Department of Chemistry and Department of Physics & Astronomy, University of California Irvine, Irvine, California 92697, United States; ocid.org/0000-0002-6015-3135; Email: smukamel@uci.edu

Authors

Jérémy R. Rouxel — Department of Chemistry and Department of Physics & Astronomy, University of California Irvine, Irvine, California 92697, United States; Université de Lyon, UJM-Saint-Étienne, CNRS, IOGS, Laboratoire Hubert Curien UMR 5516, Saint-Étienne 42023, France; orcid.org/0000-0003-3438-6370

Daniel Keefer – Department of Chemistry and Department of Physics & Astronomy, University of California Irvine, Irvine, California 92697, United States; ◎ orcid.org/0000-0001-5941-5567

Haiwang Yong — Department of Chemistry and Department of Physics & Astronomy, University of California Irvine, Irvine, California 92697, United States; ○ orcid.org/0000-0002-5860-4259

Complete contact information is available at: https://pubs.acs.org/10.1021/acs.jctc.3c00062

Author Contributions

¶S.M.C. and Y.N. contributed equally to this work.

Notes

The authors declare no competing financial interest.

ACKNOWLEDGMENTS

We gratefully acknowledge the support of the Chemical Sciences, Geosciences, and Biosciences division, Office of Basic Energy Sciences, Office of Science, US Department of Energy (DOE), through Award DE-FG02-04ER15571 (Y.N. and D.K.), and of the NSF (Grant CHE-2246379). S.M. is a fellow of the Hagler Institute for Advanced Study at Texas A&M University. J.R.R. was supported by the Labex Manutech-SISE (ANR-10-LABX-0075) of the Université de Lyon, within the program 'Investissements d'Avenir' (ANR-11-IDEX-0007) operated by the French National Research Agency (ANR). D.K. was supported by the Alexander von Humboldt foundation through the Feodor Lynen program.

ADDITIONAL NOTE

¹ For instance, when the spectral amplitude of the field envelope is a real symmetric function, the off-resonant TTS signal is antisymmetric with respect to ω_R , $S_{\text{off-res}}(-\omega_R, T) = -S_{\text{off-res}}(\omega_R, T)$.

REFERENCES

- (1) Worth, G. A.; Cederbaum, L. S. Beyond Born-Oppenheimer: molecular dynamics through a conical intersection. *Annu. Rev. Phys. Chem.* **2004**, *55*, 127–158.
- (2) Domcke, W.; Yarkony, D. R.; Köppel, H. *Conical intersections*; Advanced Series in Physical Chemistry; World Scientific: Singapore, 2011; Vol. 17; pp i–xiii.
- (3) Polli, D.; Altoè, P.; Weingart, O.; Spillane, K. M.; Manzoni, C.; Brida, D.; Tomasello, G.; Orlandi, G.; Kukura, P.; Mathies, R. A.; et al. Conical intersection dynamics of the primary photoisomerization event in vision. *Nature (London)* **2010**, *467*, 440–443.
- (4) McFarland, B. K.; Farrell, J. P.; Miyabe, S.; Tarantelli, F.; Aguilar, A.; Berrah, N.; Bostedt, C.; Bozek, J. D.; Bucksbaum, P. H.; Castagna, J. C.; et al. Ultrafast X-ray Auger probing of photoexcited molecular dynamics. *Nat. Commun.* **2014**, *5*, 4235.
- (5) Krausz, F.; Ivanov, M. Attosecond physics. Rev. Mod. Phys. 2009, 81, 163.
- (6) Calegari, F.; Sansone, G.; Stagira, S.; Vozzi, C.; Nisoli, M. Advances in attosecond science. *J. Phys. B* **2016**, 49, 062001.
- (7) Pellegrini, C.; Marinelli, A.; Reiche, S. The physics of x-ray free-electron lasers. *Rev. Mod. Phys.* **2016**, *88*, 015006.
- (8) Duris, J.; Li, S.; Driver, T.; Champenois, E. G.; MacArthur, J. P.; Lutman, A. A.; Zhang, Z.; Rosenberger, P.; Aldrich, J. W.; Coffee, R.; et al. Tunable isolated attosecond X-ray pulses with gigawatt peak power from a free-electron laser. *Nat. Photonics* **2020**, *14*, 30–36.
- (9) Maroju, P. K.; Grazioli, C.; Di Fraia, M.; Moioli, M.; Ertel, D.; Ahmadi, H.; Plekan, O.; Finetti, P.; Allaria, E.; Giannessi, L.; et al. Attosecond pulse shaping using a seeded free-electron laser. *Nature* (*London*) **2020**, *578*, 386–391.
- (10) Ebadi, H. Tracking of Azobenzene Isomerization by X-ray Emission Spectroscopy. *J. Phys. Chem. A* **2014**, *118*, 7832–7837.
- (11) Ehlert, C.; Gühr, M.; Saalfrank, P. An efficient first principles method for molecular pump-probe NEXAFS spectra: Application to thymine and azobenzene. *J. Chem. Phys.* **2018**, *149*, 144112.
- (12) Neville, S. P.; Chergui, M.; Stolow, A.; Schuurman, M. S. Ultrafast X-Ray Spectroscopy of Conical Intersections. *Phys. Rev. Lett.* **2018**, *120*, 243001.
- (13) Wolf, T. J. A.; Myhre, R. H.; Cryan, J. P.; Coriani, S.; Squibb, R. J.; Battistoni, A.; Berrah, N.; Bostedt, C.; Bucksbaum, P.; Coslovich, G.; et al. Probing ultrafast π $\pi^*/n\pi^*$ internal conversion in organic chromophores via K-edge resonant absorption. *Nat. Commun.* **2017**, *8*, 29.
- (14) Beck, A. R.; Neumark, D. M.; Leone, S. R. Probing ultrafast dynamics with attosecond transient absorption. *Chem. Phys. Lett.* **2015**, *624*, 119–130.
- (15) Geneaux, R.; Marroux, H. J. B.; Guggenmos, A.; Neumark, D. M.; Leone, S. R. Transient absorption spectroscopy using high harmonic generation: a review of ultrafast X-ray dynamics in molecules and solids. *Philos. Trans. R. Soc. A* **2019**, *377*, 20170463.
- (16) Kobayashi, Y.; Leone, S. R. Characterizing coherences in chemical dynamics with attosecond time-resolved x-ray absorption spectroscopy. *J. Chem. Phys.* **2022**, *157*, 180901.
- (17) Kowalewski, M.; Bennett, K.; Dorfman, K. E.; Mukamel, S. Catching conical intersections in the act: Monitoring transient electronic coherences by attosecond stimulated X-ray Raman signals. *Phys. Rev. Lett.* **2015**, *115*, 193003.
- (18) Keefer, D.; Schnappinger, T.; de Vivie-Riedle, R.; Mukamel, S. Visualizing conical intersection passages via vibronic coherence maps generated by stimulated ultrafast X-ray Raman signals. *Proc. Natl. Acad. Sci. U.S.A.* **2020**, *117*, 24069–24075.
- (19) Cavaletto, S. M.; Keefer, D.; Mukamel, S. High temporal and spectral resolution of stimulated x-ray Raman signals with stochastic free-electron-laser pulses. *Phys. Rev. X* **2021**, *11*, 011029.
- (20) Goulielmakis, E.; Loh, Z.-H.; Wirth, A.; Santra, R.; Rohringer, N.; Yakovlev, V. S.; Zherebtsov, S.; Pfeifer, T.; Azzeer, A. M.; Kling, M. F.; et al. Real-time observation of valence electron motion. *Nature* (London) **2010**, 466, 739–743.

- (21) Holler, M.; Schapper, F.; Gallmann, L.; Keller, U. Attosecond Electron Wave-Packet Interference Observed by Transient Absorption. *Phys. Rev. Lett.* **2011**, *106*, 123601.
- (22) Chen, S.; Bell, M. J.; Beck, A. R.; Mashiko, H.; Wu, M.; Pfeiffer, A. N.; Gaarde, M. B.; Neumark, D. M.; Leone, S. R.; Schafer, K. J. Light-induced states in attosecond transient absorption spectra of laser-dressed helium. *Phys. Rev. A* **2012**, *86*, 063408.
- (23) Chini, M.; Zhao, B.; Wang, H.; Cheng, Y.; Hu, S. X.; Chang, Z. Subcycle ac stark shift of helium excited states probed with isolated attosecond pulses. *Phys. Rev. Lett.* **2012**, *109*, 073601.
- (24) Ott, C.; Kaldun, A.; Raith, P.; Meyer, K.; Laux, M.; Evers, J.; Keitel, C. H.; Greene, C. H.; Pfeifer, T. Lorentz meets Fano in spectral line shapes: a universal phase and its laser control. *Science* **2013**, 340, 716–720.
- (25) Pertot, Y.; Schmidt, C.; Matthews, M.; Chauvet, A.; Huppert, M.; Svoboda, V.; Von Conta, A.; Tehlar, A.; Baykusheva, D.; Wolf, J.-P.; et al. Time-resolved x-ray absorption spectroscopy with a water window high-harmonic source. *Science* **2017**, *355*, 264–267.
- (26) Attar, A. R.; Bhattacherjee, A.; Pemmaraju, C. D.; Schnorr, K.; Closser, K. D.; Prendergast, D.; Leone, S. R. Femtosecond x-ray spectroscopy of an electrocyclic ring-opening reaction. *Science* **2017**, 356, 54–59.
- (27) Kobayashi, Y.; Chang, K. F.; Zeng, T.; Neumark, D. M.; Leone, S. R. Direct mapping of curve-crossing dynamics in IBr by attosecond transient absorption spectroscopy. *Science* **2019**, *365*, 79–83.
- (28) Timmers, H.; Zhu, X.; Li, Z.; Kobayashi, Y.; Sabbar, M.; Hollstein, M.; Reduzzi, M.; Martínez, T. J.; Neumark, D. M.; Leone, S. R. Disentangling conical intersection and coherent molecular dynamics in methyl bromide with attosecond transient absorption spectroscopy. *Nat. Commun.* **2019**, *10*, 3133.
- (29) Chang, K. F.; Reduzzi, M.; Wang, H.; Poullain, S. M.; Kobayashi, Y.; Barreau, L.; Prendergast, D.; Neumark, D. M.; Leone, S. R. Revealing electronic state-switching at conical intersections in alkyl iodides by ultrafast XUV transient absorption spectroscopy. *Nat. Commun.* 2020, 11, 4042.
- (30) Chang, K. F.; Wang, H.; Poullain, S. M.; Prendergast, D.; Neumark, D. M.; Leone, S. R. Mapping wave packet bifurcation at a conical intersection in CH3I by attosecond XUV transient absorption spectroscopy. *J. Chem. Phys.* **2021**, *154*, 234301.
- (31) Zinchenko, K. S.; Ardana-Lamas, F.; Seidu, I.; Neville, S. P.; van der Veen, J.; Utrio Lanfaloni, V.; Schuurman, M. S.; Wörner, H. J. Sub-7-fs conical-intersection dynamics probed at the carbon K-edge. *Science* **2021**, *371*, 489–494.
- (32) Rebholz, M.; Ding, T.; Despré, V.; Aufleger, L.; Hartmann, M.; Meyer, K.; Stooß, V.; Magunia, A.; Wachs, D.; Birk, P.; et al. All-XUV Pump-Probe Transient Absorption Spectroscopy of the Structural Molecular Dynamics of Di-iodomethane. *Phys. Rev. X* **2021**, *11*, 031001.
- (33) Severino, S.; Ziems, K. M.; Reduzzi, M.; Summers, A.; Sun, H.-W.; Chien, Y.-H.; Gräfe, S.; Biegert, J. Non-Adiabatic Electronic and Vibrational Ring-Opening Dynamics resolved with Attosecond Core-Level Spectroscopy. *arXiv preprint arXiv:2209.04330* **2022**, DOI: 10.48550/arXiv.2209.04330.
- (34) Matselyukh, D. T.; Despré, V.; Golubev, N. V.; Kuleff, A. I.; Wörner, H. J. Decoherence and revival in attosecond charge migration driven by non-adiabatic dynamics. *Nat. Phys.* **2022**, *18*, 1206–1213.
- (35) Schultze, M.; Bothschafter, E. M.; Sommer, A.; Holzner, S.; Schweinberger, W.; Fiess, M.; Hofstetter, M.; Kienberger, R.; Apalkov, V.; Yakovlev, V. S.; et al. Controlling dielectrics with the electric field of light. *Nature (London)* **2013**, 493, 75–78.
- (36) Schultze, M.; Ramasesha, K.; Pemmaraju, C. D.; Sato, S. A.; Whitmore, D.; Gandman, A.; Prell, J. S.; Borja, L. J.; Prendergast, D.; Yabana, K.; et al. Attosecond band-gap dynamics in silicon. *Science* **2014**, *346*, 1348–1352.
- (37) Lucchini, M.; Sato, S. A.; Ludwig, A.; Herrmann, J.; Volkov, M.; Kasmi, L.; Shinohara, Y.; Yabana, K.; Gallmann, L.; Keller, U. Attosecond dynamical Franz-Keldysh effect in polycrystalline diamond. *Science* **2016**, 353, 916–919.

- (38) Moulet, A.; Bertrand, J. B.; Klostermann, T.; Guggenmos, A.; Karpowicz, N.; Goulielmakis, E. Soft x-ray excitonics. *Science* **2017**, 357, 1134–1138.
- (39) Zürch, M.; Chang, H.-T.; Borja, L. J.; Kraus, P. M.; Cushing, S. K.; Gandman, A.; Kaplan, C. J.; Oh, M. H.; Prell, J. S.; Prendergast, D.; et al. Direct and simultaneous observation of ultrafast electron and hole dynamics in germanium. *Nat. Commun.* **2017**, *8*, 15734.
- (40) Nam, Y.; Montorsi, F.; Keefer, D.; Cavaletto, S. M.; Lee, J. Y.; Nenov, A.; Garavelli, M.; Mukamel, S. Time-Resolved Optical Pump-Resonant X-ray Probe Spectroscopy of 4-Thiouracil: A Simulation Study. *J. Chem. Theory Comput.* **2022**, *18*, 3075–3088.
- (41) Mukamel, S. Principles of nonlinear optical spectroscopy; Oxford University Press: New York, Oxford, 1995.
- (42) Devine, A. L.; Nix, M. G. D.; Dixon, R. N.; Ashfold, M. N. R. Near-Ultraviolet Photodissociation of Thiophenol. *J. Phys. Chem. A* **2008**, *112*, 9563–9574.
- (43) Venkatesan, T. S.; Ramesh, S. G.; Lan, Z.; Domcke, W. Theoretical analysis of photoinduced H-atom elimination in thiophenol. *J. Chem. Phys.* **2012**, *136*, 174312.
- (44) Zhang, L.; Truhlar, D. G.; Sun, S. Electronic spectrum and characterization of diabatic potential energy surfaces for thiophenol. *Phys. Chem. Phys.* **2018**, *20*, 28144–28154.
- (45) Lin, G.-S.-M.; Xie, C.; Xie, D. Three-Dimensional Diabatic Potential Energy Surfaces for the Photodissociation of Thiophenol. *J. Phys. Chem. A* **2017**, *121*, 8432–8439.
- (46) An, H.; Choi, H.; Lee, Y. S.; Baeck, K. K. Factors Affecting the Branching Ratio of Photodissociation: Thiophenol Studied through Quantum Wavepacket Dynamics. *ChemPhysChem* **2015**, *16*, 1529–1534.
- (47) You, H. S.; Han, S.; Lim, J. S.; Kim, S. K. ($\pi \pi^*/\pi \sigma^*$) Conical Intersection Seam Experimentally Observed in the S–D Bond Dissociation Reaction of Thiophenol- d_1 . *J. Phys. Chem. Lett.* **2015**, 6, 3202–3208.
- (48) An, H.; Choi, H.; Lee, Y. S.; Baeck, K. K. Factors affecting the branching ratio of photodissociation: Thiophenol studied through quantum wavepacket dynamics. *ChemPhysChem* **2015**, *16*, 1529–1534.
- (49) Lin, G.-S.-M.; Xie, C.; Xie, D. Nonadiabatic Effect in Photodissociation Dynamics of Thiophenol via the 1π π^* State. *J. Phys. Chem. A* **2018**, *122*, 5375–5382.
- (50) Lim, I. S.; Lim, J. S.; Lee, Y. S.; Kim, S. K. Experimental and theoretical study of the photodissociation reaction of thiophenol at 243 nm: Intramolecular orbital alignment of the phenylthiyl radical. *J. Chem. Phys.* **2007**, *126*, 034306.
- (51) Ashfold, M. N. R.; Devine, A. L.; Dixon, R. N.; King, G. A.; Nix, M. G. D.; Oliver, T. A. A. Exploring nuclear motion through conical intersections in the UV photodissociation of phenols and thiophenol. *Proc. Natl. Acad. Sci. U.S.A.* **2008**, *105*, 12701–12706.
- (52) Yong, H.; Keefer, D.; Mukamel, S. Imaging Purely Nuclear Quantum Dynamics in Molecules by Combined X-ray and Electron Diffraction. *J. Am. Chem. Soc.* **2022**, *144*, 7796–7804.
- (53) Butterworth, S. On the Theory of Filter Amplifiers. Experimental Wireless and the Wireless Engineer 1930, 7, 536-541.
- (54) Campbell, J. L.; Papp, T. Widths of the atomic K-N7 levels. *At. Data Nucl. Data Tables* **2001**, *77*, 1–56.
- (55) Keefer, D.; Mukamel, S. Selective Enhancement of Spectroscopic Features by Quantum Optimal Control. *Phys. Rev. Lett.* **2021**, 126, 163202.
- (56) Chang, K. F.; Wang, H.; Poullain, S. M.; González-Vázquez, J.; Bañares, L.; Prendergast, D.; Neumark, D. M.; Leone, S. R. Conical intersection and coherent vibrational dynamics in alkyl iodides captured by attosecond transient absorption spectroscopy. *J. Chem. Phys.* **2022**, *156*, 114304.
- (57) Trebino, R.; DeLong, K. W.; Fittinghoff, D. N.; Sweetser, J. N.; Krumbügel, M. A.; Richman, B. A.; Kane, D. J. Measuring ultrashort laser pulses in the time-frequency domain using frequency-resolved optical gating. *Rev. Sci. Instrum.* **1997**, *68*, 3277–3295.
- (58) Nam, Y.; Keefer, D.; Nenov, A.; Conti, I.; Aleotti, F.; Segatta, F.; Lee, J. Y.; Garavelli, M.; Mukamel, S. Conical Intersection Passages

- of Molecules Probed by X-ray Diffraction and Stimulated Raman Spectroscopy. J. Phys. Chem. Lett. 2021, 12, 12300–12309.
- (59) Werner, H.-J.; Knowles, P. J.; Knizia, G.; Manby, F. R.; Schütz, M. Molpro: a general-purpose quantum chemistry program package. *WIREs Computat. Mol. Sci.* **2012**, *2*, 242–253.
- (60) Reiter, S.; Keefer, D.; de Vivie-Riedle, R. Quantum Chemistry and Dynamics of Excited States; Wiley: New York, 2020; pp 355-381.
- (61) Thallmair, S.; Roos, M. K.; de Vivie-Riedle, R. Design of specially adapted reactive coordinates to economically compute potential and kinetic energy operators including geometry relaxation. *J. Chem. Phys.* **2016**, *144*, 234104.
- (62) Neville, S. P.; Stolow, A.; Schuurman, M. S. Formation of electronic coherences in conical intersection-mediated dynamics. *J. Phys. B* **2022**, *55*, 044004.
- (63) Tal-Ezer, H.; Kosloff, R. An accurate and efficient scheme for propagating the time dependent Schrödinger equation. *J. Chem. Phys.* **1984**, *81*, 3967–3971.

□ Recommended by ACS

Cascade Infrared Thermal Photon Emission

Klavs Hansen, Yoni Toker, et al.

MARCH 26, 2023

THE JOURNAL OF PHYSICAL CHEMISTRY A

READ 🗹

Single-Color Isomer-Resolved Spectroscopy

Grite L. Abma, Daniel A. Horke, et al.

JUNE 01, 2022

THE JOURNAL OF PHYSICAL CHEMISTRY A

READ 🗹

Nonadiabatic Dynamics Studied by Liquid-Jet Time-Resolved Photoelectron Spectroscopy

Zachary N. Heim and Daniel M. Neumark

DECEMBER 08, 2022

ACCOUNTS OF CHEMICAL RESEARCH

READ 🗹

Femtosecond X-ray Liquidography Visualizes Wavepacket Trajectories in Multidimensional Nuclear Coordinates for a Bimolecular Reaction

Jong Goo Kim, Hyotcherl Ihee, et al.

MARCH 18, 2021

ACCOUNTS OF CHEMICAL RESEARCH

READ 🗹

Get More Suggestions >